Published in final edited form as:
Curr Med Imaging Rev. 2011 November ; 7(4): 313–327. doi:10.2174/157340511798038639.

Recent results in nonlinear strain and modulus imaging

Timothy J. Hall[1], **Paul Barbone**[2], **Assad A. Oberai**[3], **Jingfeng Jiang**[1], **Jean Francois Dord**[2], **Sevan Goenezen**[3], and **Ted G. Fisher**[1]

[1]Medical Physics Department, University of Wisconsin, Madison, Wisconsin 53706

[2]Mechanical Engineering, Boston University, 110 Cummington St, Boston, MA 02215

[3]Mechanical, Aerospace, and Nuclear Engineering, Rensselaer Polytechnic Institute, 110 8th St, Troy, NY 12180

Abstract

We report a summary of recent developments and current status of our team's efforts to image and quantify *in vivo* nonlinear strain and tissue mechanical properties. Our work is guided by a focus on applications to cancer diagnosis and treatment using clinical ultrasound imaging and quasi-static tissue deformations. We review our recent developments in displacement estimation from ultrasound image sequences. We discuss cross correlation approaches, regularized optimization approaches, guided search methods, multiscale methods, and hybrid methods. Current implementations can return results of high accuracy in both axial and lateral directions at several frames per second.

We compare several strain estimators. Again we see a benefit from a regularized optimization approach. We then discuss both direct and iterative methods to reconstruct tissue mechanical property distributions from measured strain and displacement fields. We review the formulation, discretization, and algorithmic considerations that come into play when attempting to infer linear and nonlinear elastic properties from strain and displacement measurements. Finally we illustrate our progress with example applications in breast disease diagnosis and tumor ablation monitoring. Our current status shows that we have demonstrated quantitative determination of nonlinear parameters in phantoms and *in vivo*, in the context of *2D* models and data. We look forward to incorporating *3D* data from *2D* transducer arrays to noninvasively create calibrated *3D* quantitative maps of nonlinear elastic properties of breast tissues *in vivo*.

I. INTRODUCTION

Excellent reviews of the early history of elasticity imaging are presented elsewhere in this Special Issue and will not be presented at length here. We do, however, consider our efforts to be an extension of work dating back to the early 1980's [1]–[3] where tissue mechanical properties were inferred by using ultrasound signals to monitor displacements resulting from physiological stimuli [1], [2] or compensating for undesirable physiological motion among multiple images [3]. Our work also builds on the first attempts to form strain images [4] which was facilitated by the improvements in hardware over that used by the earlier investigations. We also build on the early attempts to reconstruct elastic modulus distributions from displacement estimates (combined with other boundary conditions information) such as the work from Kallel and Bertrand [5].

Several other research groups have taken steps to exploit the potential of nonlinear elasticity imaging. Skovoroda and coworkers pioneered this direction a few years ago [6]–[8], until Skovoroda's untimely death. They focused largely on studying changes in strain contrast with overall applied strain. Their treatment of quantitative reconstruction [6] accounts for large deformation, but assumes a linear (neoHookean) stress-strain law. Nitta and Shiina [9],

on the other hand, present “nonlinear elasticity” images that show tissue nonlinear stiffening. These represent the slope of the Young’s modulus with strain, based on two assumptions not made in Skovoroda’s work: stress is uniaxial and constant, and the stress-strain law is quadratic. Thus their images may be thought of as rescaled strain-slope images.

Another approach involves nonlinear propagation of shear waves [10], [11]. A key challenge of this technique is overcoming the strong attenuation of shear waves which significantly dampens nonlinear effects. Finally, the recent work by Samani and coworkers [12]–[14] deserves mention here. These lay a strong foundation to motivate spatial reconstruction of nonlinear elastic properties.

This review highlights the progress of the collaborative efforts among the coauthors and is not an extensive review of the field of elasticity imaging in general or even of the more narrow field of quasi-static elasticity imaging. The manuscript is, in part, a historical overview of our work. But more importantly, it provides a background for why we are approaching the elasticity imaging problem in this particular manner.

In the following section we describe our work in studying methods for inducing quasi-static deformation. Section III reviews our efforts in displacement estimation from ultrasound echo signals and the related system development efforts including the development of a reliable metric to judge the “quality” of strain images in unknown media (human tissues). High quality displacement estimates are a required input into our methods of estimating the modulus distribution and those methods are reviewed in Sections V and VI. Some results of our initial applications of these techniques are reported in Sections VI and VII followed by some concluding remarks.

II. INDUCING QUASI-STATIC DEFORMATION

Both single step or piece-wise slow but continuous – potentially cyclic – deformations have been used to induce motion for elasticity imaging. However, in a practical sense, we assume as a first approximation that tissue being imaged remains in quasistatic equilibrium before and after deformations are applied. Quasi-static deformation is likely the most conceptually simple method of inducing motion for elasticity imaging. It is simple to model in computational analysis and to perform in carefully controlled laboratory experiments (see, for example, [15] and [16]). Uniaxial motion is desirable since our typical motion tracking methods (see Section III) are most sensitive to motion along the acoustic beam. The acoustic pressure field has amplitude and phase modulation in the direction of the acoustic beam but varies only in amplitude in the perpendicular (azimuthal and elevational) directions. The lack of phase information, along with the more coarse spatial sampling in the perpendicular directions, greatly reduces the accuracy and increases the variance of displacement estimates perpendicular to the acoustic beam [17]. Therefore, most methods for inducing motion in quasi-static elastography attempt to create uniaxial deformation parallel to the beam line.

Although laboratory fixtures, particularly those with stepper motors, make controlled deformations of simple materials (e.g., phantoms) quite easy, most clinical applications of quasi-static compression techniques require freehand scanning (typical of clinical ultrasound imaging exams). For example, pressing on a breast with an ultrasound transducer can produce unpredictable motion that must be monitored to control. Obtaining tissue motion that approximates the desired uniaxial deformation using freehand scanning requires real-time feedback to the user to control the direction of transducer motion. This requirement created the need for real-time displacement tracking algorithms integrated into the imaging system as described in the next section. A key finding from our initial work was that a strain image frame rate of at least 4f/s was required to provide sufficient feedback to the user to control in vivo motion and obtain consistent high quality strain images [18].

III. DISPLACEMENT AND STRAIN ESTIMATION

A significant part of our research has focused on efforts to develop methods for real-time motion tracking for *in vivo* tissues during freehand scanning in parallel with efforts to develop methods to judge motion tracking accuracy especially for *in vivo* applications where "ground truth" is unknown. Developing a real-time strain imaging system that offers instant feedback to the operator (*i.e.* high frame rate and high quality strain images) is essential for clinical use. Otherwise, obtaining consistent high quality elasticity information can be quite difficult [19].

A. Motion Tracking

With few exceptions [20]–[22], the vast majority of motion tracking techniques using ultrasound signals are correlation based. Therefore, echo signal decorrelation limits their ability to accurately track motion. Echo signal decorrelation due to gross motion/deformation could be reduced by signal processing such as temporal stretching [23], [24] or companding [15], [16]. Global companding or stretching of the post-compression echo signal by a fixed stretch factor can compensate for gross motion/deformation but requires an estimate of the applied compression and may only work well for relatively uniform media. Although adaptive stretching [24] that relies on varying the stretch factor according to the local strain can be done for inhomogeneous media, it is likely too computationally intensive to produce real-time or near real-time elasticity images in a clinical setting.

Early work has demonstrated that 1D tracking may fail to correctly track motion with deformations as small as 0.6% axial strain [16]. To achieve real-time image formation while maintaining acceptable image quality, the strain imaging algorithm must be not only computationally efficient but also robust enough to track complex *in vivo* tissue motion at least in *2D*. Our group developed a scheme now known as the "guided search strategy".

This strategy enables multi-dimensional motion tracking for imaging large (*e.g.* 1%) tissue deformation in real-time [25]. We selected the framework of block-matching algorithms as our basis for algorithm implementation because of its simplicity and flexibility for multi-dimensional motion tracking. The basic assumption of the guided search strategy is that an initial exploratory search can first be applied to selected/pre-determined locations and then certain prediction strategies may be employed to advance the estimation process from one point to its neighbors (*e.g.* as simple as a row-to-row or "axial" guidance [25]) assuming tissue motion is continuous. Using neighboring displacements as guidance, the predictive search reduces the computational demands by about 90% [25] by limiting the search range to as small as one radiofrequency (RF) sample in each direction. The method typically works well with data from modern clinical ultrasound imaging systems because the spatial sampling interval (within the image plane) is small compared to the correlation length of the imaging system point spread function (adjacent samples are highly correlated – an accurate displacement estimate for any sample is a good prediction of the displacement for its immediate neighbors). The unfortunate downside of the guided search strategy is the potential cascading errors, i.e. displacement estimate errors may provide incorrect guidance and then create downstream errors through bad guidance. One of the keys for a guided search is to make sure that large tracking errors due to false correlation peaks ("peak hopping errors" [26]) are eliminated. After iterations of designing ad hoc error detection and correction schemes [25], [27], we cast this effort into a more rigorous mathematical framework known as motion regularization.

The basic idea is that "peak hopping" errors randomly occur and thus do not satisfy motion continuity constraint when tissue is deformed as a continuum [28], [29]. To regularize the

estimated deformation field, motion tracking can be modeled as an optimization problem using a cost function combining signal correlation and a smoothness constraint as follows,

$$COST = \iint_{\Omega} (\alpha E_C + \Phi(E_S))\, d\Omega \quad (1)$$

where α is an adaptively chosen scale factor, E_C is a measure of ultrasound signal similarity and E_S is the a measure of local motion smoothness. Some early investigations into this approach [30]–[32] were implemented as iterative techniques and are therefore too slow to meet our goal of producing real-time strain images. Thus, we [28], [29], among others [33], [34], implemented an optimization method named the Viterbi algorithm [35] to more efficiently solve Eqn.(1). Our initial work [28] attempted to use regularized motion tracking (*i.e.* Eqn.(1)) for the central column of the region of interest (ROI) followed by a guided search utilizing displacement vectors obtained along the central column (hereafter referred to as the "lateral-guidance" approach). Later on, we extended the use of regularized motion tracking onto an evenly-spaced coarse grid covering the entire ROI (hereafter referred to as the "multi-grid approach") in conjunction with multi-resolution motion tracking. We found that the multi-grid approach [29] performed significantly better in numerous tests at the expense of a slower frame rate (approximately a factor of 9). Because of that reduction in computational efficiency, the multi-grid algorithm is only a near real-time algorithm (1–2 frames/second). Furthermore, our work [29] has also explored how to adjust the relative contributions to the overall cost function (Eqn. (1)) between the signal correlation and the smoothness constraint by using different forms of the smoothness function to apply various levels of the motion continuity constraint. Although it is still under development, we think a new direction for motion tracking may be "organ-specific" system design. For instance, for motion tracking around breast lesions, motion continuity is expected and therefore should be enforced. However, in situations where irregular motion can be expected, such as when large vessels are present, when there is an inter-organ boundary (*e.g.*, liver, kidney and prostate) or when there is an intra-organ cavity (*e.g.,* uterine cavity and common carotid artery), only minimal constraints are needed.

The new motion tracking algorithm reported by Chen and colleagues [36] captured our attention. They introduced a remarkably simple but very effective guided search strategy where a sorted list was used to ensure that the highest quality initial displacement estimates (hereafter referred as to "seeds") obtained from the exploratory search carry priority in guiding subsequent motion tracking. We quickly realized that, in Chen's approach [36], a "brute-force" search was used to generate initial seeds and therefore the underlying reliability of those seeds is unknown. Using a regularized motion tracking method and additional tests to improve the quality of, and confidence in, these initial seeds (hereafter referred to as the "hybrid method"), we should be able to improve the outcome of their novel guided search scheme. Our initial results [37] show that this new hybrid method performs comparably to the multi-grid approach but offers significantly higher frame rates (a factor of 8 for 1% frame-average strain).

In an example using a tissue mimicking phantom [38], shown in Figure 1, it is easy to see that *1D* tracking fails to correctly track motion in a tissue-mimicking phantom undergoing axial deformation of 1.5% strain, whereas the *2D* tracking performs very well with only occasional mistakes (*i.e.* "peak-hopping" errors). Although the *2D* "axialguidance" algorithm [25] is computationally efficient, it sometimes suffers from the "cascade error artifact" which in this image starts at the top right corner and propagates through the entire axial extent of the image. In our testing, the new hybrid approach appears to be a good balance between the speed and the image quality.

Volumetric ultrasound data acquisition is now available from clinical and prototype imaging systems to form *3D* strain images [39]–[42] (see Sec. IV). Consequently, it is logical to anticipate that the availability of volumetric echo data and subsequent full *3D* motion tracking will significantly reduce echo signal decorrelation induced by tissue motion/deformation in the elevational direction that cannot be accurately tracked in *2D* echo data. For instance, initial results [42] using data acquired by a *2D* CMUT prototype transducer [43] on a tissue-mimicking phantom have demonstrated that full *3D* tracking can provide significantly higher quality strain images (measured by the contrast-to-noise ratio and the motion tracking accuracy) compared to other *2D* or pseudo-*3D* tracking strategies.

Since ultrasound echo data are discretely sampled, variants of the classic block-matching algorithm described above likely lead to the correct RF sample-level locations between the pre- and post-deformation echo data. To obtain displacements with the sub-sample accuracy in the framework of a block-matching algorithm, the most straightforward approach is to use an interpolation function to predict the “true” correlation peak from a discretely sampled correlation function. Since the underlying correlation function is not known, any adopted interpolation function could lead to biased estimates for the sub-sample displacement. In the literature, the grid slopes algorithm [44] has shown to be relatively unbiased in comparison with the use of other conventional interpolation functions such as cosine [45], cubic spline [44] and parabolic [46] functions.

In most ultrasound strain imaging systems, the displacements perpendicular (lateral) to the ultrasound beam are estimated only because they are necessary for accurate motion tracking (see Fig. 1). Given the time constraints of real-time imaging, axial and lateral sub-sample displacements are commonly obtained through two separate interpolations. Work from several groups has independently shown that coupling of the sub-sample estimation for the axial and the lateral directions can significantly improve the accuracy of sub-sample estimation both for the axial and lateral directions. Konofagou and Ophir [47] proposed an approach where both axial and lateral displacements, estimated separately during the sub-sample estimation, can be used to re-correlate ultrasound echo signals that are iteratively compensated for motion using the most recent axial and lateral displacement estimates. In recent work, Brusseau et al. [48] mathematically formalized the local *2D* motion/deformation as an affine transformation and then jointly solved all parameters including the axial and lateral translations using a constrained nonlinear programming technique. Ebbini [49] elegantly proved that, in the vicinity of the true correlation peak, magnitude vectors of the correlation function are orthogonal to its zero-phase contours. With this observation, he developed a phase-based tracking method to simultaneously determine sub-sample displacements. A novel method developed by Viola and Walker [50] provides an alternate approach to the sub-sample estimation problem. They first use *1D* cubic splines to define a continuous representation of the reference *1D* echo signal in time domain, then determine the *1D* displacement with sub-sample accuracy by minimizing an analytic matching function between the reference and the target (pre- and post-deformation) signals. Viola and Walker have extended their method for multi-dimensional tracking [51] and this extension makes their method a coupled sub-sample estimated algorithm as well.

We are developing a simple alternative to couple the axial and the lateral sub-sample estimation. It is worth noting that all four methods mentioned above were designed as general purpose displacement estimation algorithms for multi-dimensional tracking without explicit constraints of either global or local motion continuity. Consequently, these approaches could suffer from “peak-hopping” errors when the deformations are large (as in quasi-static elasticity imaging). However, our sub-sample estimation method (described below) is based on the hybrid motion tracking algorithm described above, so it would be less likely to contain “peak-hopping” errors. More specifically, to simultaneously calculate sub-

sample estimates for a given displacement vector whose integer values are known, we first calculate a correlation function with improved spatial resolution (*e.g.* 0.02mm [lateral] × 0.002mm [axial]) in the vicinity of the correlation peak and then estimate an iso-contour near the correlation peak of this up-sampled correlation function. Modeling the ultrasonic imaging system with linear systems theory (*e.g.* [52]), suggests the shape of the iso-contour is elliptic and the center of the iso-contour is the true correlation peak. Consequently, to obtain the axial and lateral sub-sample estimates, we fit the iso-contour to an ideal ellipse to obtain its center coordinates. Conceptually, extending this approach to 3D motion tracking, fitting an ellipsoid to the *3D* iso-surface simultaneously estimates sub-sample displacements in all three directions. More details of the implementation and validation of this method are forthcoming [53]. Furthermore, during the calculation of the up-sampled correlation function described above, all search kernels from which the local correlation values are calculated can be deformed to locally compensate for known deformation (e.g. *1D* compressive loading and shearing).

Results in Fig. 2 demonstrate how coupled sub-sample estimation could improve both the axial and lateral displacements obtained by the hybrid approach using quadratic interpolation versus the coupled sub-sample estimation. The general appearance of the axial and lateral displacement and axial strain images obtained with the new sub-sample estimation method is smoother compared to results from the hybrid approach. It is interesting to note that the lateral displacement image using the new coupled estimation method seems more consistent with landmarks visible in the B-mode image (see Fig. 1), *i.e.* the gross appearance of the target. Although this new coupled sub-sample estimation algorithm is numerically intensive, all sub-sample estimations are entirely independent once their integer estimates are known. Thus, this coupled sub-sample estimation algorithm [53] may be ideally suited for parallel processing using graphic processing units (GPUs).

B. Strain Estimation

Although considerable effort has been devoted to improve the accuracy of motion tracking as described above, it is inevitable that displacement estimates contain noise. Calculation of local strains (*i.e.* gradient of the displacement field) through a simple finite difference scheme, such as a two-point forward scheme, acts like a high-pass filter and amplifies noise in the estimated displacements. The resultant strain image is often too noisy to be clinically useful. To improve the quality of strain estimation, researchers [54] investigated the use of wavelet-based methods to reduce the displacement noise prior to the strain estimation. Wavelet shrinkage, a spatially adaptive image denoising method, can be employed to remove Gaussian uncorrelated noise while retaining discontinuity details of the displacement data. To reduce the apparent noise in strain images, another simple method is to average strain estimates over time [23]. However, simple averaging trades either temporal or spatial resolution for the improved strain signal-to-noise ratio.

The most popular strain estimator is a least-squares estimator [55]. This approach estimates *1D* local strains by linearly fitting local *1D* displacements within a spatial window to a line whose slope is the calculated strain value. Luo et al. [56] presented a unified approach using the concept of a low-pass digital differentiator to study the tradeoffs among several known strain estimators. In a more general mathematical framework, the numerical differentiation can be treated as an optimization problem to obtain a strain curve $s(x)$ as follows [57],

$$F(S)=\beta\|R(S)\|^2+\|As-d\|^2 \rightarrow \min \quad (2)$$

where x is one of the dimensions of the object being imaged (for example, depth along the acoustic beam when estimating 'axial' strain), $R(s(x))$ is a regularization term that penalizes irregularity of the estimated strain $s(x)$, β is a regularization parameter, $d(x)$ is the integrated

displacement from the starting point up to $L(x)$ and, $A(s(x))$ is an antidifferentiation operator defined as follows [57],

$$A(s)+d(0)=\int_0^L s(x)dx+d(0)=d(L) \quad (3)$$

The process of obtaining a regularized strain curve $s(x)$ balances the regularity of the strain curve (*i.e.* the first term in the right hand side of Eqn. (2)) and the fidelity of displacement estimates (*i.e.* the second term in the right hand side of Eqn. (2)) during the minimization of $F(s)$. Recently, we implemented the total variational differentiation (TVD) strain estimator originally proposed by Chartrand [57]. More specifically, an R term in Eqn. (2) is chosen to penalize small local variations while allowing for discontinuous solutions.

As shown in Fig. 3-(b) below, a strain curve was estimated from simulated displacements (Fig. 3-(a)) along an Aline using three different approaches: 1) two-point forward finite difference method, 2) least-squares strain estimator with a window length of 0.2mm and 3) a TVD strain estimator where the regularization parameter β is 10. This figure clearly shows that both the least-squares strain estimator and the TVD strain estimator produce less noisy strain estimates, whereas the 2-point finite difference scheme will greatly amplify the noise in the displacement estimates and therefore is not acceptable for clinical use. Currently, our work uses the framework presented in Eqn. (2) as a unified way to optimize the strain estimation.

C. Performance Metrics

Like many new diagnostic imaging systems, phantom development [38], [58], [59], in particular, the development of anthropomorphic phantoms [59], has aided in testing prototype strain imaging systems and potentially uncovering weaknesses in these systems. However, we found that many strain imaging algorithms perform well and show great promise in phantom experiments (with regular geometry and simple boundary conditions) but fail to live up to expectations in *in vivo* clinical trials because the underlying motion in phantom experiments is too simple and uniform whereas that found in *in vivo* tissue motion during clinical trials has significantly heterogeneous mechanical properties and complex boundary conditions. Consequently, alongside this technical development in motion tracking and strain estimation algorithms, there has been a progression in the understanding of strain image quality facilitating the development of predictive theories for the design and enhancement of ultrasonic strain-imaging systems.

In early work [26], [60]–[66], attention was focused on estimating lower bounds on error variance for (time-delay and) displacement estimation, because measuring tissue motion plays a critical role in strain imaging as described above. That work collectively demonstrated that the minimum error achievable in axial strain estimates is predictable, once the strain processing and ultrasound system parameters (i.e., bandwidth, center frequency, tracking window length Z and window separation distance ΔZ) are known. Varghese and Ophir [66] proposed a quantity named the elastographic SNR_e they defined as the ratio of the mean value of the estimated strains and their standard deviation. The theoretical behavior of SNR_e – which is based on these minimum error variance bounds as a function of axial strain – is similar to a band-pass filter; therefore, the analysis result was called a “strain filter”.

These theoretical efforts collectively led to better designs for strain imaging systems in general but are inadequate for applications like ours for several important reasons. First, the derivation of the minimum error variance bounds assumes that all residual motion tracking

errors are sub-sample jitter. This is a good assumption for applications such as radiation-force experiments [67], [68] where deformations are small compared to the acoustic wavelength. But axial strain in our applications, in particular imaging tissue nonlinear parameters, are typically 1 or 2% from frame-to-frame. Tissue deformations like ours include maximum displacements of several wavelengths and potentially involve “peak-hopping” errors. Second, these minimum error variance bounds predict the limit on the best possible result in a statistical sense when an unbiased time-delay estimation algorithm is used. However, in medical image formation where accuracy in a single observation is important, we found that descriptions of anticipated image noise like the strain filter [66] are insufficient to assess the quality for a specific strain image. Third, the methods used to derive these error bounds assume *1D* correlation techniques, but our methods generally employ *2D* tracking kernels that include correlated data. The effects of correlation within the tracking kernel were not accounted for in the reported work. These combined inadequacies provided motivation for the development of an empirical metric to assess the fidelity of strain image formation in an individual basis.

A displacement quality metric (DQM; [69]) can be calculated for each strain image in a sequence. The DQM is the product of the normalized cross-correlation coefficient among the entire pre-deformation and motion-compensated post-deformation RF echo fields and the normalized cross-correlation coefficient between two consecutive motion-compensated strain images [69]. The rationale behind developing this empirical metric is briefly justified below. First, by applying the displacement estimates to the deformed echo data and remapping to the coordinates of the pre-deformation echo data field, we can register the two RF echo fields. A higher normalized cross correlation (NCC) value between two registered regions implies that two regions with apparent deformations are better registered. Hence, it may be surmised that displacement estimates between the two RF fields are more accurate. Second, for small frame-to-frame deformations (e.g. 1%), the local strain is dependent on the local tissue stiffness (possibly corrupted by uncorrelated noise). Thus, high NCC between two consecutive strain images means similarity and relatively low noise among both strain images, and thereby suggests better strain image quality. By multiplying these two NCC values we obtain a DQM value that is automatically normalized, with 1 providing the best possible result, and provides a fidelity measure of the process of strain image formation. In several of our recent studies, we have demonstrated that the DQM method can be used for automated data selection to reduce user-dependency during clinical studies [70], data selection for modulus reconstruction [71] or comparison among different motion tracking algorithms involving *in vivo* data [27]–[29].

IV. EXTENSIONS TO *3D* ELASTICITY IMAGING

Most of our previous work with clinical imaging systems employed *1D* array transducers to obtain *2D* RF echo fields, displacement fields and strain fields. However, more recently we have investigated extensions of our motion tracking algorithms to *3D* data fields from *2D* linear arrays [39], [42] and from mechanically rocked *1D* arrays [39], [40]. While the mechanically rocked *1D* arrays are commercially available, they are less desirable for quasi-static elasticity imaging for several reasons. First, they tend to be relatively low frequency (intended for use in abdominal imaging) which also reduces the absolute bandwidth – both of which increase the lower bound on displacement estimate error variance [26]. Second, the mechanically rocked *1D* arrays typically have a curved contact surface which induces a complex stress and strain pattern at the contact surface [72] that can complicate the motion. Third, these array systems typically provide sector-shaped RF echo fields which complicates the interpretation of “axial strain”. Example strain images obtained with a prototype 9MHz *2D* CMUT linear array [42] and obtained with a 5MHz mechanically rocked *1D* array (C7F2 fourSight), both operated by the Siemens SONOLINE Antares (Siemens Healthcare,

Ultrasound Business Unit, Mountain View, CA, USA) and imaging the same phantom, are shown in Fig. 4. Modulus reconstruction obtained from the displacement fields from the *2D* CMUT array were recently reported [42].

V. DIRECT INVERSION TANGENT MODULUS RECONSTRUCTION

We have also developed a simple linear inversion technique to obtain the spatial distribution of elastic moduli given the displacements and force measurements along boundaries [73]. In this approach, the conventional procedures of displacement-based finite element analysis (FEA) are used to construct a linear system of equations as follows,

$$KU=F \tag{4}$$

where K, U and F are the system stiffness matrix, displacement vector and force vector for a discretized elastic object, respectively. In conventional forward FEA solutions, the stiffness value for each (finite) element is known and the displacement vector (see Eqn. (4)) will be solved for given certain boundary conditions. In this linear inversion process, we rewrite the left hand side of Eqn. (4) using the Young's modulus distribution as explicit variables while assuming all displacements can be measured. In other words, this process makes the spatial distribution of modulus values the unknown vector in a new linear system of equations. Given appropriate force boundary conditions, the solution of this new linear system is very straightforward. In the initial publication [73] the modulus distribution was solved in a least-squares sense and therefore the solution was sensitive to the noise level in the displacement vector as expected. However, the performance of this method could be improved if a constrained least-squares solver is used. It is also worth noting that the new linear system for the inverse problem is a redundant system (i.e. more equations than the unknowns). Consequently, future work includes reducing the required measurements similar to approaches used in compressed sensing.

VI. RECONSTRUCTING NONLINEAR ELASTIC MODULUS

For this review, we outline the issues surrounding nonlinear modulus reconstruction from measured strain fields. Many of these issues are identical to those that occur in linear modulus reconstruction. Others, while not identical, have their counterparts in linear elastic modulus reconstruction. Still others are unique to the problem of nonlinear modulus estimation.

The section is organized roughly linearly in terms of the decisions and modeling choices that must be made in tackling the reconstruction problem. In each case, we describe the options we have chosen and give justification for those choices. While we believe they are good choices, the methodology we have developed by no means represents the only way, nor even necessarily the best way, to solve the problem. It does, however, seem to represent a feasible path to obtaining practical results that we believe will prove useful in the clinic.

In the next part of this section, we first describe the choice of the mathematical model used to describe breast tissue deformation. Our recent focus has been on a modified Veronda-Westman model for incompressible tissue in plane stress. Given that model, we next discuss the data requirements to determine the modulus distribution unambiguously. Then we discuss the iterative computational solution of the inverse problem within the context of nonlinear modulus inversion. We close with computational examples, and a brief discussion of current research directions.

A. Mathematical modeling

Though we live in a three-dimensional world, most clinical ultrasound scanners today provide two dimensional images. This situation is in a rapid state of flux, and indeed, we are currently translating all our work to *3D*. Up to now, however, most of our applications have been based on *2D* data. There are two main *2D* approximations of *3D* deformation, plane stress and plane strain. The accuracy of either can be questioned when applied to *3D* deformations, but plane stress offers significant advantages when it comes to inversion. For one thing, the forward plane stress problem is better conditioned for incompressible materials. For plane strain, special treatment of incompressibility is required even to get a good forward solution. For plane stress, no such special treatment is required. A second advantage to plane stress is that the inverse problem is better posed. For the linear elastic inversion, a single deformation gives the modulus distribution up to a multiplicative constant. For plane strain, a single deformation gives rise to a family of possible modulus distributions. The relative accuracy of these two assumptions is demonstrated with a later example.

We also make the assumption that the tissue behaves as an incompressible solid. Given that soft tissues comprise mobile fluid components, this assumption may be justifiably questioned. In evaluating this assumption, one must take account of the time scales of deformation, the time scales of observation, and the time scales of fluid redistribution within the tissue. By our estimates [74], with compression and observation times on the order of one to several seconds, fluid redistribution most likely has a negligible effect on the tissue deformation patterns.

The nonlinear stress-strain behavior of breast tissue is thought to be determined largely by the collagen network which provides the main tissue structure. Like soft tissues, such networks exhibit a large “toe” region of compliant behavior at low strains, followed by a relatively steep increase in the stress after the network “locks”. Several models have been proposed in the literature to capture such behavior. Three popular choices are the Yeoh model, the Arruda-Boyce model [75], and the Veronda-Westmann model [76]. O’Hagan and Samani [14] have fit these, along with others, to the mechanical behavior of breast tissue, and found satisfactory agreement with all of them. Of these various options, we have relied most heavily upon a modified Veronda-Westmann model.

The Veronda-Westmann model was introduced in 1970 [76] to model the observed exponential stiffening of skin tissue. In our early work [77] we introduced a simplified Veronda-Westmann that reduces the original three parameters to just two. These two parameters represent the shear modulus at zero strain, and the exponential stiffening parameter. The recent results of O’Hagan and Samani [14] indicate that our original choice is suboptimal in three respects. First, though all models give satisfactory performance they report more accurate fits from the Yeoh and Ogden models. Second, the best fitting three-parameter Veronda-Westmann model is inconsistent with the simplified two-parameter model that we have chosen. Third, for incompressible materials, the Veronda-Westmann model does not give a purely deviatoric stress tensor. Therefore, we are currently using an exponential model due apparently to Blatz and coworkers [78].

B. Data requirements

The exponential model we currently use to represent the nonlinear behavior of phantoms and tissues is:

$$W=\frac{\mu}{2\gamma}\left(e^{\gamma\left[J^{-\frac{2}{3}}I_1-3\right]}-1\right) \tag{5}$$

Here, W represents the strain-energy density (energy per unit volume), μ is the shear modulus at zero strain, and γ represents the degree of nonlinearity, or exponential growth rate of stress with strain. The symbols I_1 and J are strain measures, given by:

$$I_1=\lambda_1^2+\lambda_2^2+\lambda_3^2 \tag{6}$$

$$J=\lambda_1\lambda_2\lambda_3 \tag{7}$$

and $\lambda_1, \lambda_2, \lambda_3$ are the principle stretches of the material. If we denote by $\varepsilon = \Delta L/L$ the change in length divided by the initial length, then the stretch is λ = final length/original length = $(L + \Delta L)/L = 1 + \varepsilon$. Thus, in an undeformed material, the strain is zero, and $\lambda_1 = \lambda_2 = \lambda_3 = 1$. In an incompressible material, which we assume, $J \equiv 1$. In an inhomogeneous material, $\mu(X)$ and $\gamma(X)$ are functions of (original) position in the material.

In uniaxial tension, this model leads to the following stress-strain relation:

$$\sigma=\mu\left(\lambda^2-\frac{1}{\lambda}\right)\exp\left[\gamma\left(\lambda^2-\frac{2}{\lambda}\right)\right] \tag{8}$$

$$\approx 3\mu\varepsilon\exp\lfloor 3\gamma\varepsilon^2\rfloor \tag{9}$$

At small strains where ε^2 is negligible, this model predicts linear elastic incompressible behavior with shear modulus μ. Therefore, if we confine our attention to very small (i.e. linear) strains, we can determine μ as if the material is linear elastic. For plane stress conditions, this means that a single small-strain deformation determines the entire spatial distribution of $\mu(X)$, up to a multiplicative constant [79]. Currently the uniqueness theory for γ is underdeveloped, but initial calculations based on uniaxial stress conditions imply that γ may be determined absolutely from two different large deformation strain field measurements.

C. Computational formulation

We treat the inverse problem as an optimization problem. The goal is to find the material parameter distribution that, when used in a forward model of the experiment, predicts the measurements as closely as possible. Such a description might fit any number of approaches, however, and so here we briefly discuss some of the features of our particular approaches.

The objective function we seek to optimize is:

$$\pi[\mu,\gamma]=\pi_{data}+\frac{1}{2}\alpha_1 R_1(\mu)+\frac{1}{2}\alpha_2 R_2(\gamma) \tag{10}$$

Here, π_{data} is the data matching functional, and R_1 and R_2 are regularization functionals. This objective is minimized as a function of $\mu(X)$ and $\gamma(X)$ under the constraint that the predicted displacement fields u^i satisfy the equations of equilibrium.

The data matching functional is how we define what is meant by “match the measurement as closely as possible.” Typically we know the measurements more accurately in the ultrasound

axial direction than in the ultrasound lateral (or elevational) directions (see Sec. II). Therefore, it makes sense to place greater confidence in the axial measurements than in the lateral. Hence we choose for our data matching functional:

$$\pi_{data}=\frac{1}{2}\sum_{i=1}^{n_{meas}} w_i \left\| T(u^i) - T(u^i_{meas}) \right\|_0^2 \tag{11}$$

We choose the matrix T *a priori* to weight different components of the displacement field different amounts, depending upon our confidence in those measures. Statistical estimation theory for Gaussian distributed uncertainties suggests that $T \propto diag[\sigma_j^{-1}]$ [80], [81].

The regularization terms enforce *a priori* knowledge of the probability distribution of the modulus. They help control the impact of noise on the reconstruction, and improve the conditioning of the optimization problem. It is worthwhile emphasizing that they enforce (read "impose") *a priori* assumptions on the modulus distribution. If a strong Tikhonov regularization is used on the modulus derivatives, any inclusion will be reconstructed as a smooth bump, regardless of its original profile. Similarly, a strong total variation (TV) regularization will yield an inclusion with sharp sides, again regardless of the inclusion's actual profile. A desirable feature of TV regularization is its ability to preserve sharp boundaries at interfaces.

In practice, we usually use a weak and regularized TV regularization. This is given by the equation:

$$R(\mu)=\int_\Omega \sqrt{\nabla\mu\cdot\nabla\mu+\beta^2}\,d\Omega \tag{12}$$

Total variation regularization is achieved in the limit of $\beta \to 0$. In this limit, however, the regularization functional is singular at $\nabla\mu = 0$. Therefore, we use a small nonzero β. We have recently noticed that the convergence behavior of the iterative optimization algorithm is strongly dependent on the smallness ofβ.

Our experience indicates that for reasonable regularization levels, the optimization functional is well behaved, and so local search methods work efficiently. The BFGS (Broyden-Fletcher-Goldfarb-Shanno [82], [83]) is a gradient based method that gradually builds an approximate Hessian with each iteration, and converges satisfactorily quickly for these problems. We prefer gradient based methods, since the adjoint method can be used to efficiently compute the gradient.

Iterative optimization methods require the forward solution for each of several different material property distributions. In the nonlinear elasticity inverse problem, a typical iteration of the inverse problem proceeds as follows. Instead of the current guess for the material properties, one solves the forward problem to compute the "predicted" displacement field. The BFGS algorithm is used to obtain an updated guess of the parameter values, based upon the function value, its (current) gradient, and past history. Then one solves the linearized "adjoint problem" in order to compute the gradient of the optimization functional. As the adjoint problem is linear, the dominant computational cost is thus clearly in the solution of the nonlinear forward problem. This is traditionally solved by a continuation method from zero loading to the full nonlinear loading. In this application, however, one can use a continuation method in the material properties from the previous material property distribution. This typically yields convergence of the forward problem in a very few Newton iterations.

The final key ingredient required for the successful computational solution of this inverse problem is an appropriate, stable, forward discretization method. The key issue here is dealing efficiently with the incompressibility of the material. Whether the effective Poisson's ratio of the tissue is taken to be exactly 1/2 or some close approximation like 0.49, standard FEM formulations are inadequate. The key issue is to avoid mesh locking at reasonable mesh sizes. In our experience, some solutions of the locking problem yield impractically small load step requirements for the forward problem. Recently we have implemented the stabilized FE method described in [84]. This gives accurate solutions and converges well with large load steps (i.e. large material property steps). This work is described in [85].

D. Sample results

We begin with an example that shows the benefits of *3D* inversion over *2D* inversions. The reconstructions were obtained from the *3D* phantom data described in [86]. Figure 5 shows a vertical slice from the *3D* reconstruction through the center of the phantom. We see a stiff layer along the top and a stiff inclusion about 5mm in size, of the same stiffness as the layer. When the displacement fields from this single slice are used in plane stress or plane strain reconstructions, the modulus fields shown in Figures 6(a) and 6(b) result, respectively. We note from these figures that the plane stress reconstruction is much more faithful to the more accurate *3D* reconstruction. Nevertheless, the *2D* plane stress reconstruction shows artifacts resulting from the *3D* nature of the displacement field. One of these is an artificial enhancement of the stiffness in the upper stiff layer. A second related artifact is the appearance of a stiff horizontal layer along the bottom edge. Both of these are recognized as being due to a combination of sticking of phantom at the boundaries, which is exacerbated by the incompressibility of the material. The peak inclusion stiffness of about 2.7 is correctly identified in the plane stress reconstruction.

We next show the results of reconstructions from two *in vivo* clinical datasets. These are both *2D* datasets reconstructed under of the assumption that plane stress conditions applied. In neither case do we have calibration data to determine the shear modulus, so the shear modulus reconstruction is relative. The gamma parameter, however, is calibrated and therefore may be interpreted as quantitative. These parameters refer to the reduced Veronda-Westmann strain energy density function described in [87]. Figure 7 shows the (relative) shear modulus μ and nonlinear parameter γ for a fibroadenoma.

In the shear modulus image, we see an apparently stiff, small nodule in the lower left that we believe to be an artifact due to noisy strain measurements. The fibroadenoma itself is the light green oval shape on the left, whose outline is traced in the right hand figure. In simulated and phantom data, we have seen boundary condition errors create stiff surface layer artifacts, which may explain the apparently stiff layer at the skin surface in this reconstruction. We note the stiffness (i.e. shear modulus, μ) contrast is roughly 10:1, while γ is no larger than about 10. It is assumed at this point that the red region in the γ reconstruction is an artifact, but whether due to model error, boundary conditions, or noisy data is not known.

Figure 8 shows the reconstructed shear modulus and nonlinear elasticity parameter for an invasive ductal carcinoma. The shear modulus image shows a kidney bean shaped region of elevated stiffness, with a contrast of roughly 10:1. Thus, this stiffness is not considerably different from that of the fibroadenoma. By contrast, however, the nonlinear parameter γ is highly elevated. Most of the lesion is characterized by a value of $\gamma \geq 30$. So far, in about ten cases studied, we have seen a marked contrast between the reconstructed values of γ in a fibroadenoma and the reconstructed values of γ in an invasive ductal carcinoma.

Though our clinical data so far is limited to *2D*, we continue to work toward the goal of full calibrated *3D* modulus and nonlinear elastic reconstructions. Extending the methodology to *3D* is nontrivial. At a minimum, it requires appropriate treatment of incompressibility in the forward model. Several treatments we have tried interact poorly with the inverse iterations. More problematic, however, is the conditioning of the *3D* inverse problem. It is more analogous to the plane strain problem than to the plane stress problem (*c.f.* Figure 6). Nevertheless, *3D* reconstructions of linear shear modulus from phantom data are reported in [86], [88]. Here, we show (Fig. 9) the results of *3D* nonlinear reconstructions performed with simulated data. The "measured"displacement field was generated by solving the forward problem with a specified material distribution and adding 3% white noise. The exact distribution comprises of a hard, strain hardening inclusion in a soft background with a contrast of 1:5 in the shear modulus and the nonlinear parameter. The reconstructions are able to recover this contrast quite well.

E. Current directions

Our current directions are aimed at automating the processing steps and making the inversion process more efficient. At the moment, this effort takes two specific and related directions: controlling and improving the convergence of the iterative process, and automating the choice of the regularization parameters.

We have found that the rate of convergence of the iterative inversion depends on both the type of regularization and the choice of regularization parameters. Tikhonov regularization, perhaps because it gives a nicely convex contribution to the objective function, gives rise to quite fast convergence. Total variation regularization, on the other hand, has a less predictable impact on the convergence behavior, and can be an order of magnitude slower. Furthermore, the convergence, and to a lesser extent the result, can depend upon the choice of β(see equation (12)). We are currently working on identifying the appropriate scaling to select β(andα, the overall regularization parameter) to ensure both accurate results and efficient convergence.

Next steps include developing an adjoint formulation that does not require a priori knowledge of the problem boundary conditions. While the adjoint formulation for the optimization problem depends upon these boundary conditions [89], the inverse problem itself does not [90].

VII. APPLICATIONS

A. Clinical trials of strain imaging in breasts

A multi-observer, multi-institution study of breast elasticity imaging was conducted based on the first-generation fully-integrated real-time elasticity imaging system [18]. The details of the conduct and results of that study are reported by Burnside, et al. [70]. Several significant findings are worth noting. First, the overall results suggest that, even in that early stage of strain imaging system development, elasticity image information interpreted by highly trained breast radiologists (who were also specifically trained in strain image interpretation) significantly improved their ability to assess the risk of breast cancer for 98 biopsy-confirmed cases. (Combining results for three radiologists, the area under the receiver operating characteristic curve for B-mode imaging alone was 0.876. The area increased to 0.903 when strain images were displayed simultaneously with B-mode.) Second, the confidence of the observers interpretation increased with increased strain image quality, but observer variability significantly lowered the overall performance in elasticity image interpretation (in some cases the radiologists were unable to determine if they were observing high-quality strain images or just visually pleasing strain images). That finding prompted our investigations into a robust metric for strain image quality (see Sec. III).

Significant improvements in strain imaging systems (those currently commercially available) and a quantitative measure of strain image quality should significantly reduce observer variability in image interpretation and increase observer performance in assessing breast cancer risk. This is an ongoing area of investigation.

B. Ablation monitoring

Thermal ablation is a medical procedure where tumor or some dysfunctional tissue (*e.g.* heart) is ablated using external thermal energy to treat a medical disorder. Radiofrequency (RF) ablation [91], one of most popular thermal ablation techniques, has become increasingly accepted in the last 15 years with promising results in treating hepatic tumors. Its application for cancer therapy has now been expanded into neoplasmas in bones, kidneys, lungs and breasts. While thermal ablation can be an effective cancer treatment tool, the lack of a reliable imaging modality to monitor progression of ablation treatment is still a significant problem [91]–[94]. Unfortunately, because of a lack of adequate imaging-based treatment monitoring options, undertreated portions of the tumor often go undetected until follow-up. In clinical practice, ultrasound is less effective in depicting the actual boundaries of a thermal ablation zone while repeated CT dosage becomes an issue both for patients and physicians. MR is less frequently used because of the low availability of interventional MR scanners and the lack of MR-compatible ablation equipment. Consequently, the local recurrence rate, a technical term for treatment efficacy, varies widely ranging from 33–55% under ultrasound guidance [93], [95].

During RF ablation, protein denaturation during heating results in an increase in the elastic modulus of tissue [96]. Therefore, thermal ablation zones appear to be stiffer than surrounding untreated tissue and may be differentiated by new elasticity imaging methods that directly estimate mechanical properties of soft tissue. Our group is developing an elastic modulus imaging (EMI) method for visualizing thermal ablation zones. Compared to modulus inversion methods developed for breast imaging (Sections V and VI), this method is designed for using ablation applicatorinduced deformation [97]. Consequently, the displacements induced by the the needle-like applicator are treated as the source of mechanical stimulus and enforced during the solution of the forward problem.

In our recent pre-clinical animal study [98], we compared the radiological/pathological correlation and accuracy of this technique in 14 in vivo thermal ablation zones created in normal porcine livers. We found that comparison of elastic modulus imaging measurements and gross pathology measurements showed high correlation with respect to the area of thermal ablation zones (Pearson coefficient = 0.950 and $p < 0.0001$). The radiological/pathological correlation was lower (correlation = 0.853, $p < 0.0001$) for strain imaging among same ablation zones. More importantly, elastic modulus images provided higher (more than a factor of 2) contrast-to-noise ratios for evaluating these thermal ablation zones than those on corresponding strain images, thereby reducing inter-observer variability. Unlike strain, elastic modulus images are not dependent on the assumption of uniform stress distribution, thereby providing unambiguous information regarding tissue elasticity [99].

Figure 10 provides an example reconstruction where elastic modulus imaging shows superior visualization compared to strain imaging. The calculated CNRs were 0.55 and 4.65 for the strain (10(b)) and elastic modulus (10(c)) images, respectively. Three contours of the thermal ablation zone depicted by three human observers in the corresponding strain image have nearly no overlap, thereby demonstrating poor visibility using strain imaging for the case investigated.

VIII. CONCLUSIONS

We, and other groups, continue to make progress in developing and testing quasi-static elasticity imaging systems. Quasi-static methods for mechanical strain imaging have gone from laboratory investigations through clinical and on to commercially available products. Relative strain images in 2D are a common part of clinical breast evaluation in many centers around the world. But, there are many opportunities for continuing development.

Great progress is being made to obtain quantitative elastic modulus and elastic nonlinearity images, instead of relative strain. Quantitative images will allow more precise communication among clinicians regard patient conditions, it will also allow direct comparison of tissue properties from one examination to the next facilitating tracking disease progression and monitoring the effects of therapy. All of this work is being extended to3D. Further, it is our vision that elastic modulus imaging could potentially provide rapid feedback to clinicians for the real-time or near real-time evaluation of the ablation zone to help reduce the number of local recurrences and subsequent re-treatment sessions after thermal tumor ablation. The future of this technology looks very bright.

Acknowledgments

We gratefully acknowledge Siemens Healthcare, Ultrasound Business Unit, Mountain View, CA, USA, for their system support and NIH support from grants R01CA100373, R21CA133488, R01CA140271 and T32CA00206. We further gratefully acknowledges contributions to the data collection and processing from Michael S. Richards (University of Rochester, Rochester, NY) and Olalekan Babaniyi (Boston University, Boston, MA). We are also grateful to Nick Hangiandreou (Mayo Clinic, Rochester, MN, USA) and Bill Svensson (Charring Cross Hospital, London, UK) for their assistance in obtaining some of the data used in our breast elasticity imaging studies.

REFERENCES

1. Dickinson RJ, Hill CR. Measurement of soft tissue motion using correlation between a-scans. Ultrasound Med Biol. 1982; 8(3):263–271. [PubMed: 7101574]
2. Wilson LS, Robinson DE. Ultrasonic measurement of small displacements and deformations of tissue. Ultrason Imaging. 1982; 4(1):71–82. [PubMed: 7199773]
3. Morrison DC, McDicken WN, Smith DS. A motion artefact in real-time ultrasound scanners. Ultrasound Med Biol. 1983; 9(2):201–203. [PubMed: 6879831]
4. Ophir J, Cespedes I, Ponnekanti H, Yazdi Y, Li X. Elastography: a quantitative method for imaging the elasticity of biological tissues. Ultrason Imaging. 1991; 13(2):111–134. [PubMed: 1858217]
5. Kallel F, Bertrand M. Tissue elasticity reconstruction using linear perturbation method. IEEE Trans Med Imag. 1996; 15(3):299–313.
6. Skovoroda AR, Lubinski MA, Emelianov SY, O'Donnell M. Reconstructive elasticity imaging for large deformations. IEEE Trans Ultrason, Ferroelec, Freq Cont. 1999; 46(3):523–535.
7. Erkamp, R.; Emelianov, SY.; Skovoroda, AR.; O'Donnell, M. Nonlinear elasticity imaging; IEEE Ultrason. Symp. Proc; 2002. p. 1891-1894.
8. Erkamp R, Emelianov SY, Skovoroda AR, O'Donnell M. Nonlinear elasticity imaging: Theory and phantom study. IEEE Trans Ultrason, Ferroelec, Freq Cont. 2004; 51(5):532–539.
9. Nitta N, Shiina T. A visualization of nonlinear elasticity property of tissues by ultrasound. Electronics and Communications in Japan Part III-Fundamental Electronic Science. 2002; 85(12):9–18.
10. Catheline S, Gennisson J, Fink M. Measurement of elastic nonlinearity of soft solid with transient elastography. J Acoust Soc Am. 2003; 114:3087. [PubMed: 14714790]
11. Sack I, Mcgowan C, Samani A, Luginbuhl C, Oakden W, Plewes D. Observation of nonlinear shear wave propagation using magnetic resonance elastography. Mag Res Med. 2004; 52(4):842–850.
12. Mehrabian H, Samani A. An iterative hyperelastic parameters reconstruction for breast cancer assessment. Proc. of SPIE 161C–1. 2008; 6916:69.

13. Samani A, Zubovits J, Plewes D. Elastic moduli of normal and pathological human breast tissues: An inversion-technique-based investigation of 169 samples. Phys Med Biol. 2007; 52(6):1565–1576. [PubMed: 17327649]
14. O'Hagan J, Samani A. Measurement of the hyperelastic properties of 44 pathological ex vivo breast tissue samples. Phys Med Biol. 2009; 54:2557–2569. [PubMed: 19349660]
15. Chaturvedi P, Insana MF, Hall TJ. 2-D companding for noise reduction in strain imaging. IEEE Trans Ultrason Ferroelectr Freq Control. 1998; 45(1):179–191. [PubMed: 18244170]
16. Chaturvedi P, Insana MF, Hall TJ. Testing the limitations of 2-D companding for strain imaging using phantoms. IEEE Trans Ultrason Ferroelectr Freq Control. 1998; 45(4):1022–1031. [PubMed: 18244257]
17. Bilgen M. Dynamics of errors in 3d motion estimation and implications for strain-tensor imaging in acoustic elastography. Phys Med Biol. 2000; 45:1565–1578. [PubMed: 10870711]
18. Hall TJ, Zhu Y, Spalding CS. In vivo real-time freehand palpation imaging. Ultrasound Med Biol. 2003; 29(3):427–435. [PubMed: 12706194]
19. Doyley MM, Bamber JC, Fuechsel F, Bush N. A freehand elastographic imaging approach for clinical breast imaging: system development and performance evaluation. Ultrasound Med Biol. 2001; 27(10):1347–1357. [PubMed: 11731048]
20. Bilgen M. Wavelet transform-based strain estimator for elastography. IEEE Trans Ultrason Ferroelectr Freq Control. 1999; 46(6):1407–1415. [PubMed: 18244336]
21. Konofagou EE, Varghese T, Ophir J, Alam SK. Power spectral strain estimators in elastography. Ultrasound Med Biol. 1999; 25(7):1115–1129. [PubMed: 10574343]
22. Hoyt K, Forsberg F, Ophir J. Analysis of a hybrid spectral strain estimation technique in elastography. Phys Med Biol. 2006; 51(2):197–209. [PubMed: 16394333]
23. Varghese T, Ophir J, Cespedes I. Noise reduction in elastograms using temporal stretching with multicompression averaging. Ultrasound Med Biol. 1996; 22(8):1043–1052. [PubMed: 9004428]
24. Alam SK, Ophir J. Reduction of signal decorrelation from mechanical compression of tissues by temporal stretching: Applications to elastography. Ultrasound Med Biol. 1997; 23(1):95–105. [PubMed: 9080622]
25. Zhu Y, Hall TJ. A modified block matching method for real-time freehand strain imaging. Ultrason Imaging. 2002; 24(3):161–176. [PubMed: 12503771]
26. Walker WF, Trahey GE. Fundamental limit on delay estimation using partially correlated speckle signals. IEEE Trans Ultrason Ferroelectr Freq Control. 1995; 42(2):301–308.
27. Jiang J, Hall TJ. A parallelizable real-time motion tracking algorithm with applications to ultrasonic strain imaging. Phys Med Biol. 2007; 52(13):3773–3790. [PubMed: 17664576]
28. Jiang, J.; Hall, TJ. A regularized real-time motion tracking algorithm using dynamics programming for ultrasonic strain imaging; IEEE Ultrason. Symp. Proc; 2006. p. 606-609.
29. Jiang J, Hall TJ. A generalized speckle tracking algorithm for ultrasonic strain imaging using dynamic programming. Ultrasound Med Biol. 2009; 35(11):1863–1879. [PubMed: 19682789]
30. Yeung F, Levinson SF, Fu D, Parker KJ. Feature-adaptive motion tracking of ultrasound image sequences using a deformable mesh. IEEE Trans Med Imaging. 1998; 17(6):945–956. [PubMed: 10048851]
31. Zhu Y, Chaturvedi P, Insana MF. Strain imaging with a deformable mesh. Ultrason Imaging. 1999; 21(2):127–146. [PubMed: 10485566]
32. Pellot-Barakat C, Frouin F, Insana MF, Herment A. Ultrasound elastography based on multiscale estimations of regularized displacement fields. IEEE Trans Med Imaging. 2004; 23(2):153–163. [PubMed: 14964561]
33. Rivaz H, Boctor E, Foroughi P, Zellars R, Fichtinger G, Hager G. Ultrasound elastography: a dynamic programming approach. IEEE Trans Med Imaging. 2008; 27(10):1373–1377. [PubMed: 18815089]
34. Petrank Y, Huang L, O'Donnell M. Reduced peak-hopping artifacts in ultrasonic strain estimation using the viterbi algorithm. IEEE Trans Ultrason Ferroelectr Freq Control. 2009; 56(7):1359–1367. [PubMed: 19574147]

35. Viterbi A. Error bounds for convolutional codes and an asymptotically optimum decoding algorithm. IEEE Transactions on Information Theory. 1967; 13(2):260–269.
36. Chen L, Treece GM, Lindop JE, Gee AH, Prager RW. A quality-guided displacement tracking algorithm for ultrasonic elasticity imaging. Med Image Anal. 2009; 13(2):286–296. [PubMed: 19081285]
37. Jiang J, Hall TJ. A fast hybrid algorithm combining regularized motion tracking and predictive search for reducing the occurrence of large displacement errors. IEEE Trans Ultrason Ferroelectr Freq Control. 2010; 58(4):730–736. [PubMed: 21507750]
38. Pavan TZ, Madsen EL, Frank GR, Carneiro AAO, Hall TJ. Nonlinear elastic behavior of phantom materials for elastography. Physics Med Biol. 2010; 55(9):2679–2692.
39. Fisher, TG.; Jiang, J.; Hall, TJ. Volumetric strain imaging; Proc. IEEE Ultrasonics Symposium; 2007. p. 355-358.
40. Bharat S, Fisher TG, Varghese T, Hall TJ, Jiang J, Madsen EL, Zagzebski JA, Lee J, T F. Three-dimensional electrode displacement elastography using the Siemens C7F2 fourSight four-dimensional ultrasound transducer. Ultrasound Med Biol. 2008; 34(8):1307–1316. [PubMed: 18374467]
41. Treece GM, Lindop JE, Gee AH, Prager RW. Freehand ultrasound elastography with a 3-d probe. Ultrasound Med Biol. 2008; 34(3):463–474. [PubMed: 17993244]
42. Fisher TG, Hall TJ, Panda S, Richards MS, Barbone PE, Jiang J, Resnick J, Barnes S. Volumetric elasticity imaging with a 2-D CMUT array. Ultrasound Med Biol. 2010; 36(6):978–990. [PubMed: 20510188]
43. Oralkan O, Ergun AS, Cheng CH, Johnson JA, Karaman M, Lee TH, Khuri-Yakub BT. Volumetric ultrasound imaging using 2-d cmut arrays. IEEE Trans Ultrason Ferroelectr Freq Control. 2003; 50(11):1581–1594. [PubMed: 14682642]
44. Geiman BJ, Bohs LN, Anderson ME, Breit SM, Trahey GE. A novel interpolation strategy for estimating subsample speckle motion. Phys Med Biol. 2000; 45(6):1541–1552. [PubMed: 10870709]
45. de Jong PG, Arts T, Hoeks AP, Reneman RS. Experimental evaluation of the correlation interpolation technique to measure regional tissue velocity. Ultrason Imaging. 1991; 13(2):145–161. [PubMed: 1858219]
46. Foster SG, Embree PM, O'Brien WR. Flow velocity profile via time-domain correlation: error analysis and computer simulation. IEEE Trans Ultrason Ferroelectr Freq Control. 1990; 37(3): 164–175. [PubMed: 18285029]
47. Konofagou E, Ophir J. A new elastographic method for estimation and imaging of lateral displacements, lateral strains, corrected axial strains and poisson's ratios in tissues. Ultrasound Med Biol. 1998; 24(8):1183–1199. [PubMed: 9833588]
48. Brusseau E, Kybic J, Deprez JF, Basset O. 2-d locally regularized tissue strain estimation from radiofrequency ultrasound images: theoretical developments and results on experimental data. IEEE Trans Med Imaging. 2008; 27(2):145–160. [PubMed: 18334437]
49. Ebbini ES. Phase-coupled two-dimensional speckle tracking algorithm. IEEE Trans Ultrason Ferroelectr Freq Control. 2006; 53(5):972–990. [PubMed: 16764451]
50. Viola F, Walker WF. A spline-based algorithm for continuous time-delay estimation using sampled data. IEEE Trans Ultrason Ferroelectr Freq Control. 2005; 52(1):80–93. [PubMed: 15742564]
51. Viola F, Coe RL, Owen K, Guenther DA, Walker WF. Multi-dimensional spline-based estimator (muse) for motion estimation: algorithm development and initial results. Ann Biomed Eng. 2008; 36(12):1942–1960. [PubMed: 18807190]
52. Rao M, Varghese T. Correlation analysis of three-dimensional strain imaging using ultrasound two-dimensional array transducers. J Acoust Soc Am. 2008; 124(3):1858–1865. [PubMed: 19045676]
53. Jiang J, Hall TJ. A coupled speckle tracking algorithm with applications in shear strain imaging. IEEE Trans Med Imag. 2010 submitted.
54. Techavipoo U, Varghese T. Wavelet denoising of displacement estimates in elastography. Ultrasound Med Biol. 2004; 30(4):477–491. [PubMed: 15121250]

55. Kallel F, Ophir J. A least-squares strain estimator for elastography. Ultrason Imaging. 1997; 19(3): 195–208. [PubMed: 9447668]
56. Luo J, Bai J, He P, Ying K. Axial strain calculation using a low-pass digital differentiator in ultrasound elastography. IEEE Trans Ultrason Ferroelectr Freq Control. 2004; 51(9):1119–1127. [PubMed: 15478973]
57. Chartrand R. Numerical differentiation of noisy, nonsmooth data. 2007
58. Hall TJ, Bilgen M, Insana MF, Krouskop TA. Phantom materials for elastography. IEEE Trans. Ultrason. Ferroelectr. Freq. Control. 1997; 44(6):1355–1365.
59. Madsen EL, Hobson MA, Frank GR, Shi H, Jiang J, Hall TJ, Varghese T, Doyley MM, Weaver JB. Anthropomorphic breast phantoms for testing elastography systems. Ultrasound Med Biol. 2006; 32(6):857–874. [PubMed: 16785008]
60. Weiss AJ, Weinstein E. Fundamental limitations in passive time delay estimation- part 1: Narrow-band systems. IEEE Trans Acoust, Speech, Signal Processing. 1983; ASSP-31(2):472–486.
61. Weinstein E, Weiss AJ. Fundamental limitations in passive time-delay estimation – part ii: Wide-band systems. IEEE Trans Acoust, Speech, Signal Processing. 1984; ASSP-32(5):1064–1078.
62. Carter, GC. Coherence and time delay estimation : an applied tutorial for research, development, test, and evaluation engineers. Piscataway, NJ: IEEE Press; 1993.
63. Cespedes I, Insana M, Ophir J. Theoretical bounds on strain estimation in elastography. IEEE Trans Ultrason Ferroelectr Freq Control. 1995; 42(5):969–972.
64. Bilgen M, Insana MF. Error analysis in acoustic elastography i. displacement estimation. J Acoust Soc Am. 1997; 101(2):1139–1146. [PubMed: 9035401]
65. Bilgen M, Insana MF. Error analysis in acoustic elastography ii. strain estimation and snr analysis. J Acoust Soc Am. 1997; 101(2):1147–1154. [PubMed: 9035402]
66. Varghese T, Ophir J. Theoretical framework for performance characterization of elastography: the strain filter. IEEE Trans Ultrason Ferroelectr Freq Control. 1997; 44(1):164–172. [PubMed: 18244114]
67. Fatemi M, Greenleaf JF. Ultrasound-stimulated vibro-acoustic spectrography. Science. 1998; 280(5360):82–85. [PubMed: 9525861]
68. Nightingale K, Scott Soo M, Nightingale R, Trahey G. Acoustic radiation force impulse imaging: in vivo demonstration of clinical feasibility. Ultrasound Med Biol. 2002; 28(2):227–235. [PubMed: 11937286]
69. Jiang J, Hall TJ, Sommer A. A novel performance descriptor for ultrasonic strain imaging: A preliminary study. IEEE Trans Ultrason Ferroelectr Freq Control. 2006; 53(6):1088–1102. [PubMed: 16846142]
70. Burnside ES, Hall TJ, Sommer AM, Hesley GK, Sisney GA, Svensson WE, Fine JP, Jiang J, Hangiandreou NJ. Differentiating Benign from Malignant Solid Breast Masses with US Strain Imaging1. Radiology. 2007; 245(2):401–410. [PubMed: 17940302]
71. Jiang J, Brace C, Andreano A, Dewall RJ, Rubert N, Fisher TG, Varghese T, Lee F Jr, Hall TJ. Ultrasound-based relative elastic modulus imaging for visualizing thermal ablation zones in a porcine model. Phys Med Biol. 2010; 55(8):2281–2306. [PubMed: 20354279]
72. Ponnekanti H, Ophir J, C´espedes I. Ultrasonic imaging of the stress distribution in elastic media due to an external compressor. Ultrasound Med Biol. 1994; 20(1):27–33. [PubMed: 8197624]
73. Zhu Y, Hall TJ, Jiang J. A finite element approach for young's modulus reconstruction. IEEE Trans Med Imag. 2003; 22(7):890–901.
74. Leiderman R, Barbone PE, Oberai AA, Bamber JC. Coupling between elastic strain and interstitial fluid flow: Ramifications for poroelastic imaging. Phys Med Biol. 2006; 51:6291–6313. [PubMed: 17148819]
75. Arruda EM, Boyce MC. A three-dimensional constitutive model for the large stretch behavior of rubber elastic materials. J Mech Phys Solids. 1993; 41(2):389–412.
76. Veronda D, Westmann R. Mechanical characterization of skin–Finite deformations. J Biomech. 1970; 3(1):111–122. [PubMed: 5521524]
77. Gokhale NH, Oberai AA, Barbone PE. Solution of the non-linear elasticity imaging inverse problem: the compressible case. Inverse Problems. 2008; 24(4)

78. Blatz P, Chu B, Wayland H. On the mechanical behavior of elastic animal tissue. J Rheol. 1969; 13:83.
79. Barbone PE, Oberai AA. Elastic modulus imaging: some exact solutions of the compressible elastography inverse problem. Phys Med Biol. 2007; 52:1577–1593. [PubMed: 17327650]
80. Keeping, ES. Introduction to Statistical Inference. New York: Dover; 1995.
81. Vogel, CR. Computational methods for inverse problems. Philadelphia: SIAM; 2002.
82. Nocedal, J.; Wright, J. Stephen, Numerical Optimization. 2nd ed.. New York: Springer-Verlag; 1999.
83. Zhu C, Byrd R, Nocedal J. L-BFGS-B: Algorithm 778: L-BFGS-B, FORTRAN routines for large scale bound constrained optimization. ACM Trans Math Software. 1997; 23(4):550–560.
84. Maniatty A, Liu Y, Klaas O, Shephard M. Higher order stabilized finite element method for hyperelastic finite deformation. Computer Methods in Applied Mechanics and Engineering. 2002; 191(13–14):1491–1503.
85. Goenezen S, Barbone PE, Oberai AA. Solution of the non-linear elasticity imaging inverse problem: the incompressible case. 2010 in preparation.
86. Richards MS, Barbone PE, Oberai AA. Quantitative three dimensional elasticity imaging from quasi-static deformation: a phantom study. Phys Med Biol. 2009; 54:757–779. [PubMed: 19131669]
87. Oberai AA, Gokhale NH, Goenezen S, Barbone PE, Hall TJ, Sommer AM, Jiang J. Linear and nonlinear elasticity imaging of soft tissue in vivo: demonstration of feasibility. Phys Med Biol. 2009; 54(5):1191–1207. [PubMed: 19182325]
88. Fisher T, Hall T, Panda S, Richards M, Barbone P, Jiang J, Resnick J, Barnes S. Volumetric Elasticity Imaging with a 2-D CMUT Array. Ultrasound Med Biol. 2010; 36(6):978–990. [PubMed: 20510188]
89. Oberai AA, Gokhale NH, Doyley MM, Bamber JC. Evaluation of the Adjoint Equation Based Algorithm for Elasticity Imaging. Phys Med Biol. 2004; 49(13):2955–2974. [PubMed: 15285258]
90. Albocher U, Oberai AA, Barbone PE, Harari I. Adjoint-weighted equation for inverse problems of incompressible plane-stress elasticity. Computer Methods in Applied Mechanics and Engineering. 2009; 198:2412–2420.
91. Goldberg SN, Gazelle GS, Mueller PR. Thermal ablation therapy for focal malignancy: a unified approach to underlying principles, techniques, and diagnostic imaging guidance. AJR Am J Roentgenol. 2000; 174(2):323–331. [PubMed: 10658699]
92. Gazelle GS, Goldberg SN, Solbiati L, Livraghi T. Tumor ablation with radio-frequency energy. Radiology. 2000; 217(3):633–646. [PubMed: 11110923]
93. Solbiati L, Ierace T, Goldberg SN, Sironi S, Livraghi T, Fiocca R, Servadio G, Rizzatto G, Mueller PR, Del Maschio A, Gazelle GS. Percutaneous us-guided radio-frequency tissue ablation of liver metastases: treatment and follow-up in 16 patients. Radiology. 1997; 202(1):195–203. [PubMed: 8988211]
94. Montgomery RS, Rahal A, Dodd r, D G, Leyendecker JR, Hubbard LG. Radiofrequency ablation of hepatic tumors: variability of lesion size using a single ablation device. AJR Am J Roentgenol. 2004; 182(3):657–661. [PubMed: 14975966]
95. Rossi S, Di Stasi M, Buscarini E, Quaretti P, Garbagnati F, Squassante L, Paties CT, Silverman DE, Buscarini L. Percutaneous rf interstitial thermal ablation in the treatment of hepatic cancer. Am J Roentgenol. 1996; 167(3):759–768. [PubMed: 8751696]
96. Kiss MZ, Varghese T, Hall TJ. Viscoelastic characterization of in vitro canine tissue. Phys Med Biol. 2004; 49(18):4207–4218. [PubMed: 15509061]
97. Jiang J, Varghese T, Brace C, Madsen E, Hall T, Bharat S, Hobson M, Zagzebski J, Lee F Jr. Young's modulus reconstruction for radio-frequency ablation electrode-induced displacement fields: A feasibility study. IEEE Trans Med Imaging. 2009; 28(8):1325–1334. [PubMed: 19258195]
98. Jiang J, Brace C, Andreano A, DeWall RJ, Rubert N, Fisher TG, Varghese T, Lee JF, Hall TJ. Ultrasound-based relative elastic modulus imaging for visualizing thermal ablation zones in a porcine model. Phys Med Biol. 2010; 55(8):2281–2306. [PubMed: 20354279]

99. Barbone PE, Bamber JC. Quantitative elasticity imaging: what can and cannot be inferred from strain images. Phys Med Biol. 2002; 47(12):2147–2164. [PubMed: 12118606]

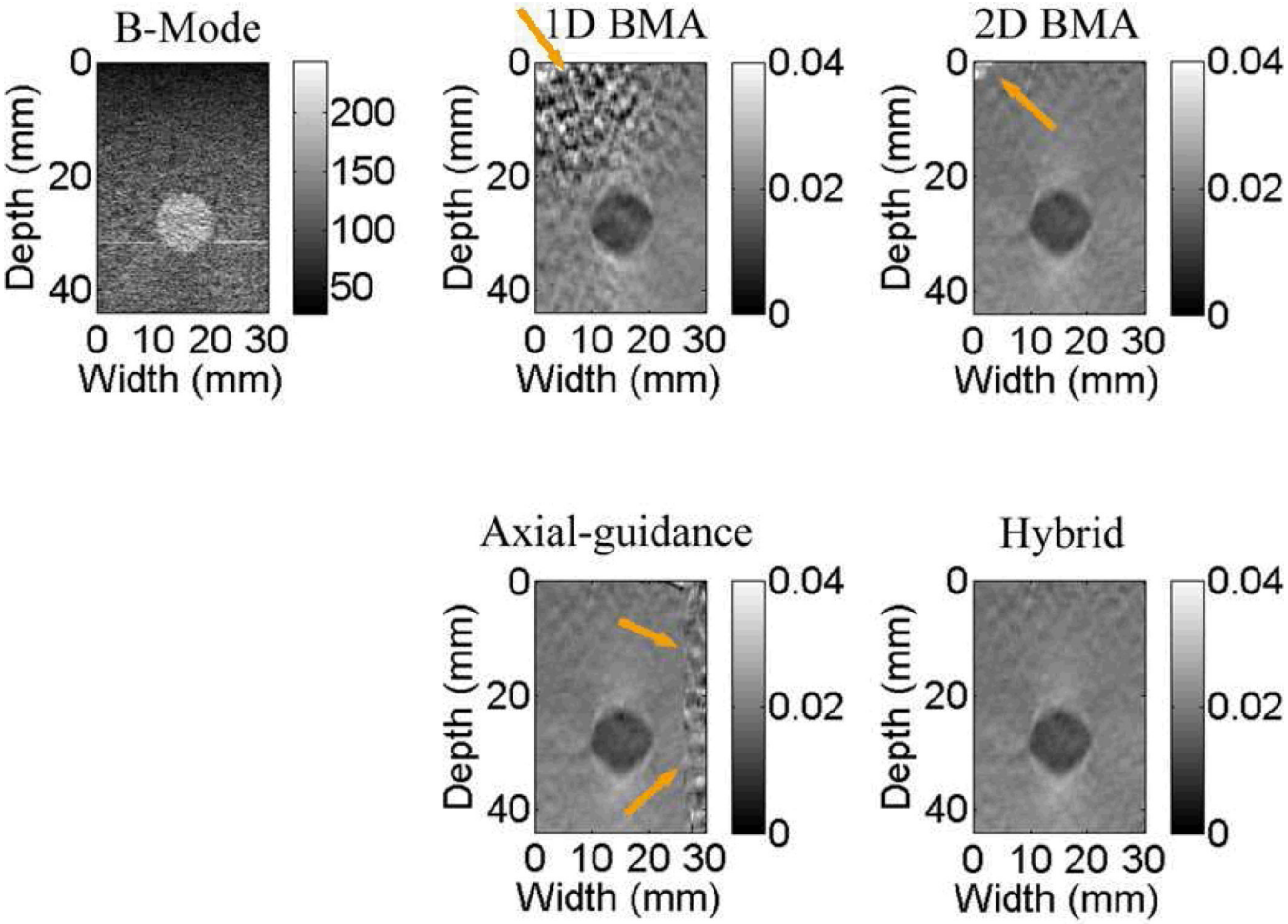

Fig. 1.

Images of B-mode and axial strain from a tissue-mimicking phantom [38] with one spherical inclusion that is approximately 2 times stiffer than the background. Local strains were estimated using four variants of block-matching algorithms (BMA). Arrows in each strain image point to locations of de-correlation noise resulting from errors due to poor motion tracking.

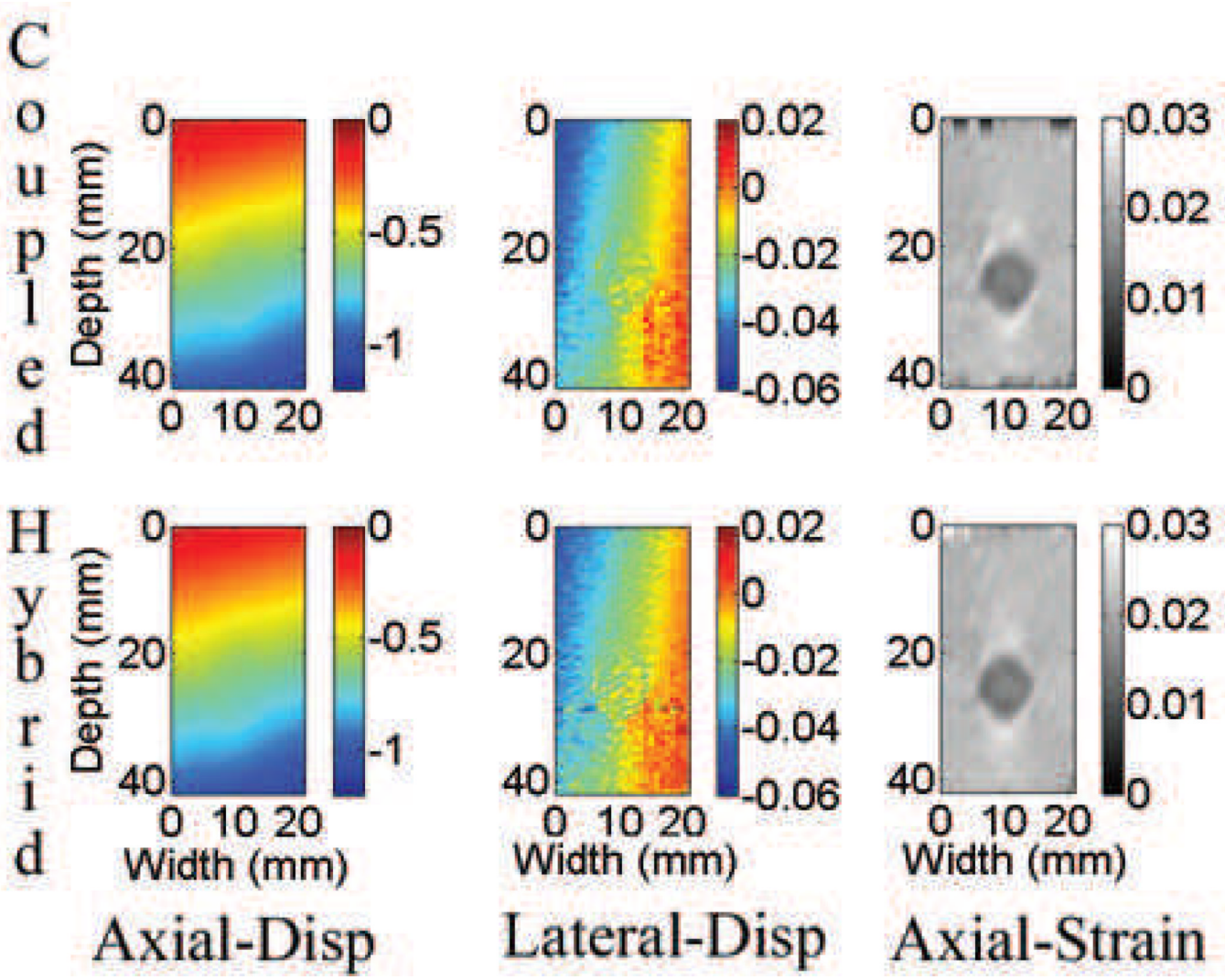

Fig. 2.
Axial and lateral displacement, and axial strain images of the tissue-mimicking phantom displayed in Fig. 1.

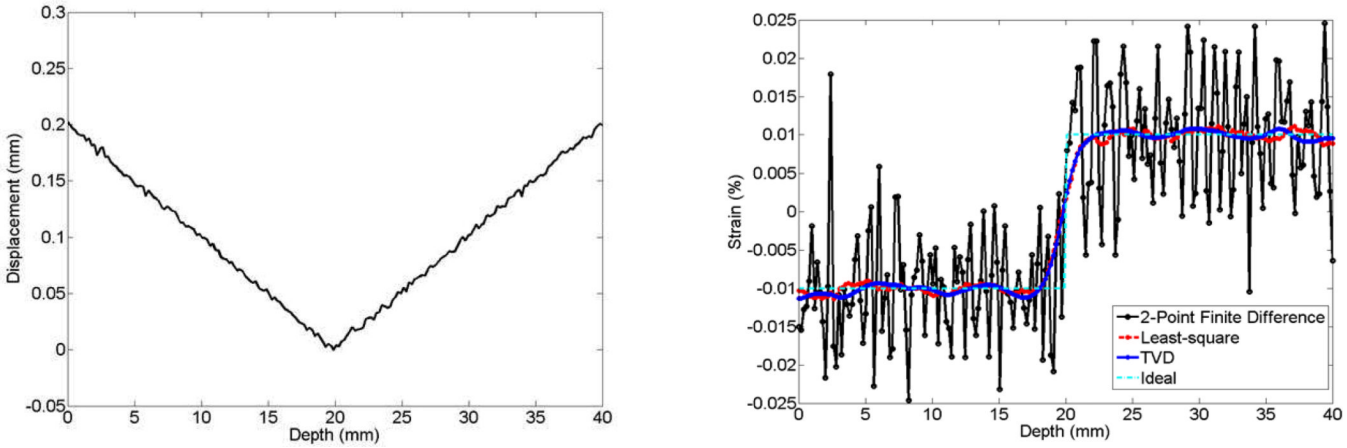

Fig. 3.

(a) Simulated displacements along an A-line and, (b) estimated strain curves using three different methods: 1) two-point forward finite difference method, 2) least-squares strain estimator with a window length of 0.2mm and, 3) a TVD strain estimator with a regularization parameter of 10. The ideal strain is also presented using a dashed line in (b).

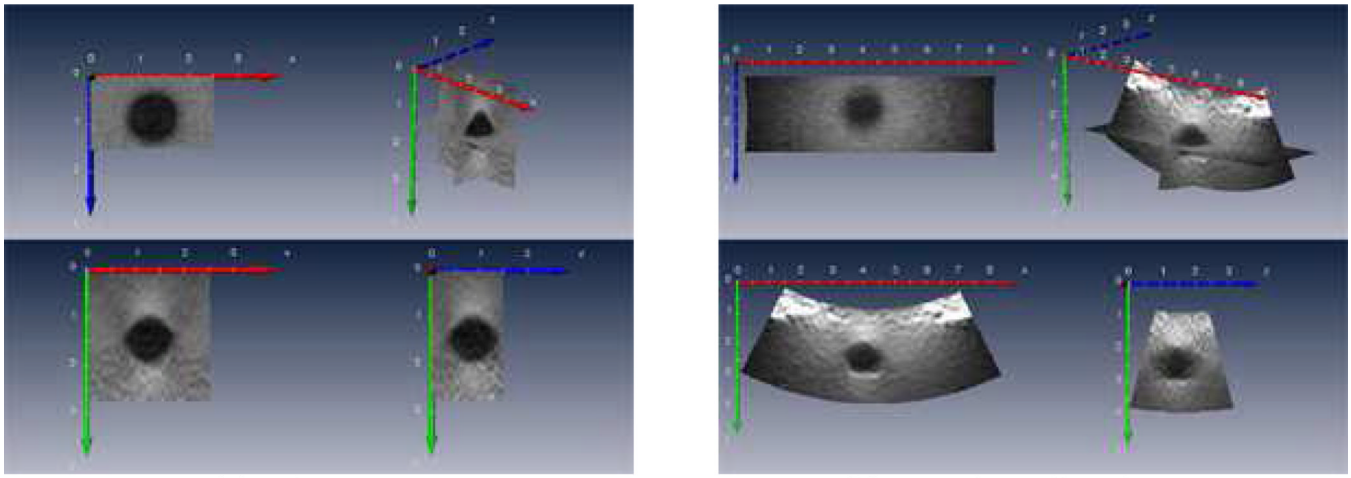

Fig. 4.

3D strain images obtained using the lateral guidance motion tracking algorithm for two methods of *3D* RF echo data acquisition. The upper left image in each composite set is the "top view" or C-scan image plane. The bottom left image is the normal "B-scan" or azimuthal image plane. The bottom right image is the elevational image plane. The top right image is the *3D* volume with cross sectional slices through each plane for visualization. Note that the *2D* array has higher center frequency than the mechanically rocked *1D* array.

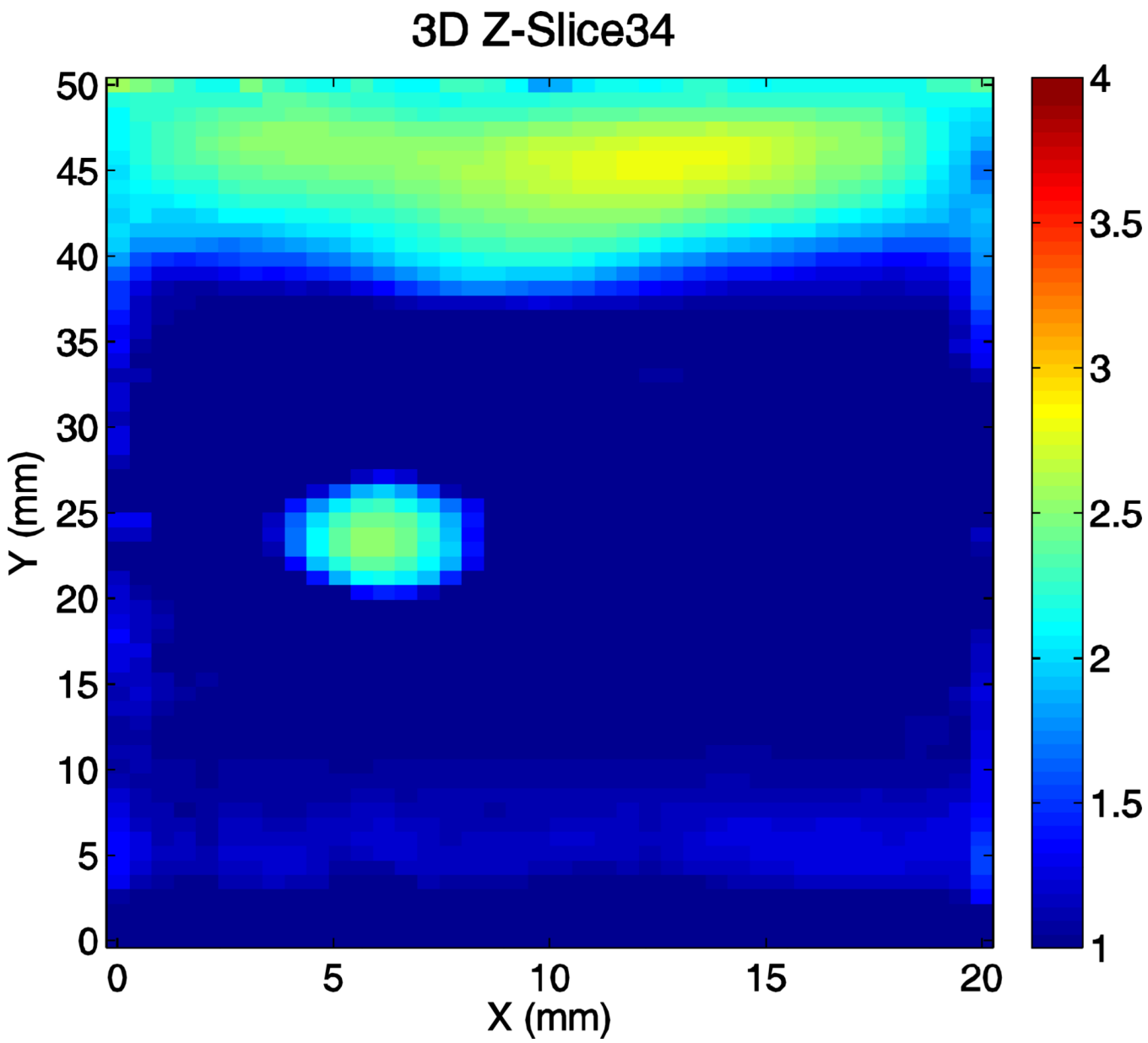

Fig. 5.

One slice from a *3D* reconstruction of linear shear modulus in a tissue mimicking phantom. Data from [86]. The phantom was manufactured to have a 1cm thick stiff layer at the top, and a 5mm inclusion of the same stiffness. (The upper 2 − 3mm of the top layer have been cropped in the processing.)

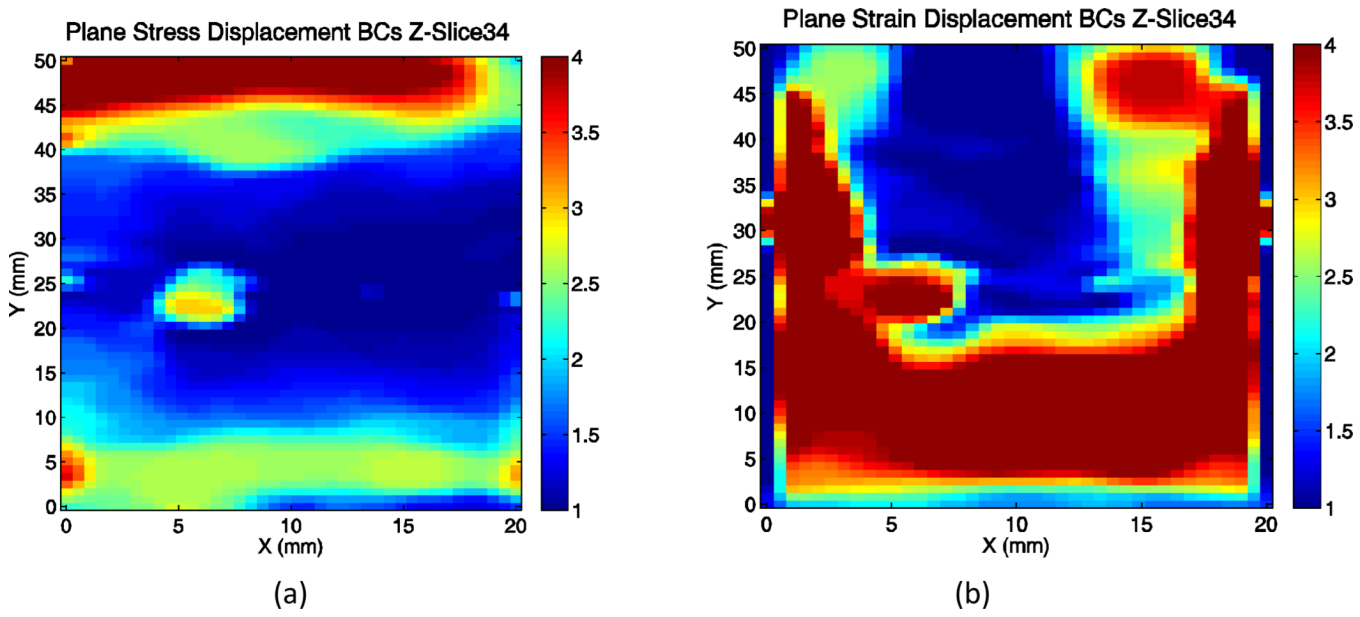

Fig. 6.

Two dimensional reconstructions of linear shear modulus in the same plane as shown in Figure 5. The left figure (a) is the linear shear modulus reconstructed using the plane stress approximation; the right figure (b) is the linear shear modulus reconstructed using the plane strain approximation. Observe that the plane stress approximation produces a more accurate reconstruction, but is nevertheless highly sensitive to boundary artifacts.

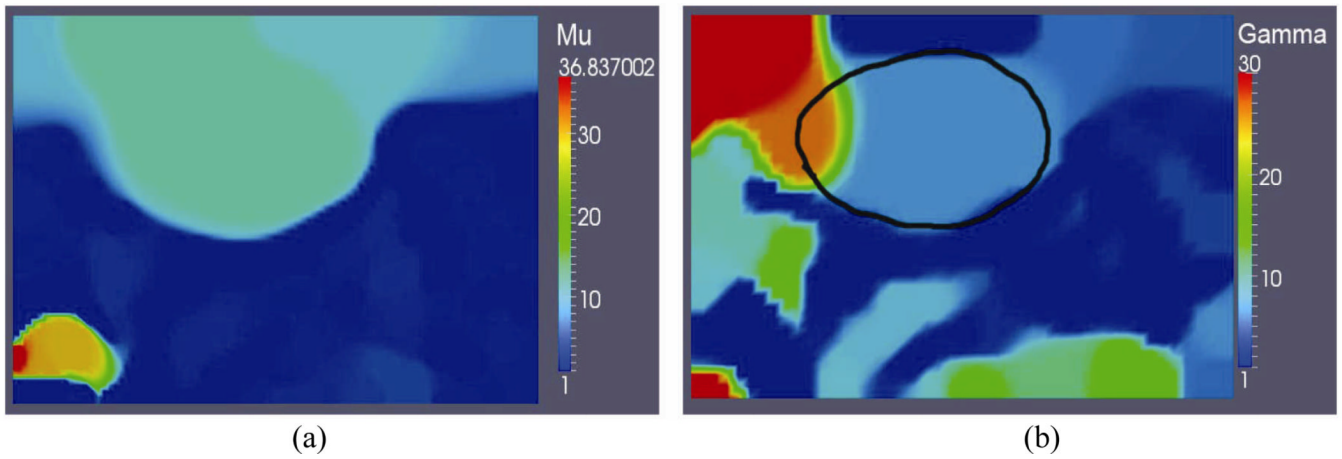

Fig. 7.

Reconstructed shear modulus distribution (a) and nonlinear elastic parameter (b) of a fibroadenoma, reconstructed from two dimensional in vivo data under assumptions of plane stress. The apparently stiff, small nodule in the lower left we believe is an artifact due to noisy strain measurements. The fibroadenoma is the light green oval shape on the left, whose outline is traced in the right hand figure. In simulated and phantom data, we have seen boundary condition errors create stiff surface layer artifacts, which may explain the apparently stiff layer at the skin surface in this reconstruction (*c.f.* Figure 6). Note the stiffness (i.e. shear modulus, μ) contrast of roughly 10:1, while γ is no larger than about 10.

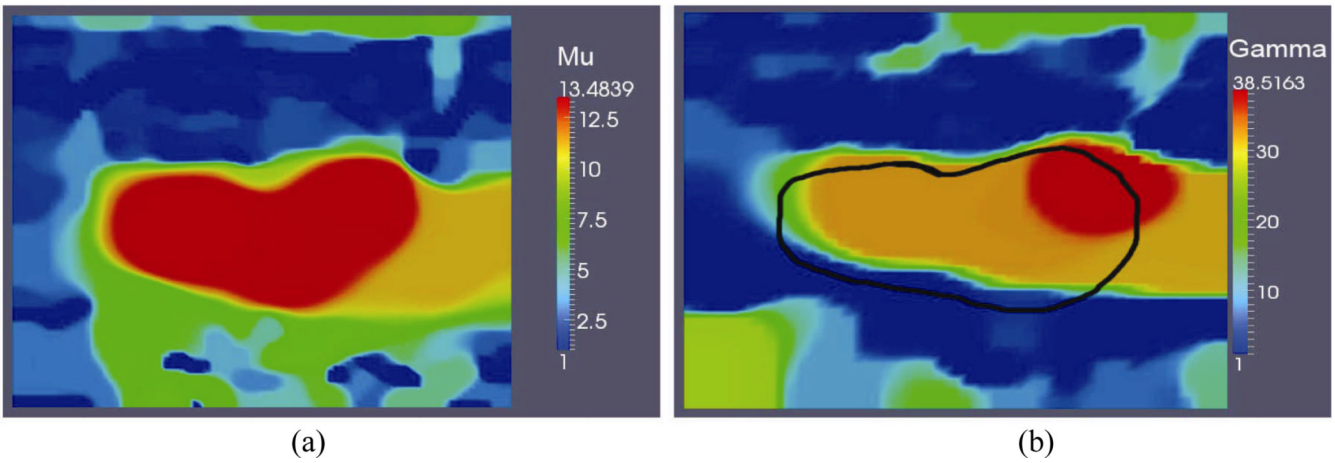

Fig. 8.

Reconstructed shear modulus distribution (a) and nonlinear elastic parameter (b) of an invasive ductal carcinoma, reconstructed from two dimensional *in vivo* data under assumptions of plane stress. Note the stiffness (*i.e.* shear modulus, μ) contrast of roughly 10:1, but here γ is significantly larger than about 30. In the ten or so cases we have so far investigated, the striking difference in γ between fibroadenomas and invasive ductal carcinomas is consistent. We note that regions showing elevated stiffness near the skin surface and in image corners are attributed to artifacts, whose origin is unknown.

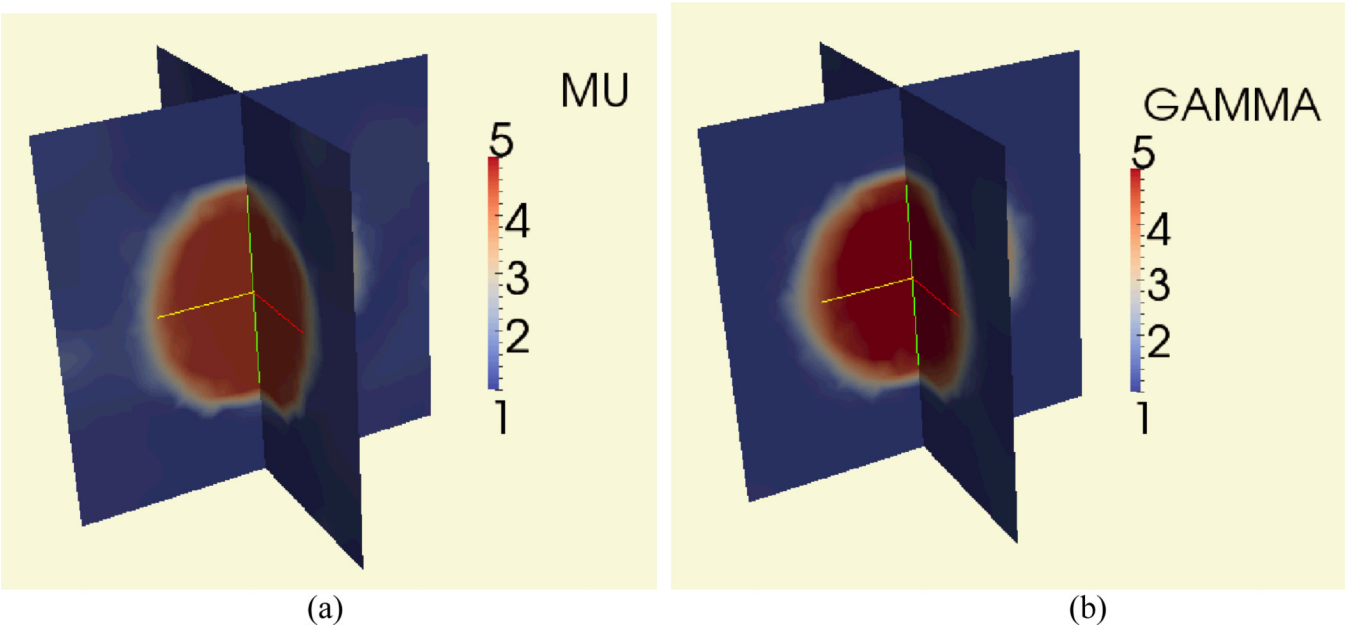

Fig. 9.

Reconstruction of the linear shear modulus (a) and the non-linear strain hardening parameter (b) for an incompressible material. The "measured" displacement field was generated by solving the forward problem with a specified material distribution and adding 3% white noise. The exact distribution comprises of a hard, strain hardening inclusion in a soft background with a contrast of 1:5 in the shear modulus and the nonlinear parameter. The reconstructions are able to recover this contrast quite well.

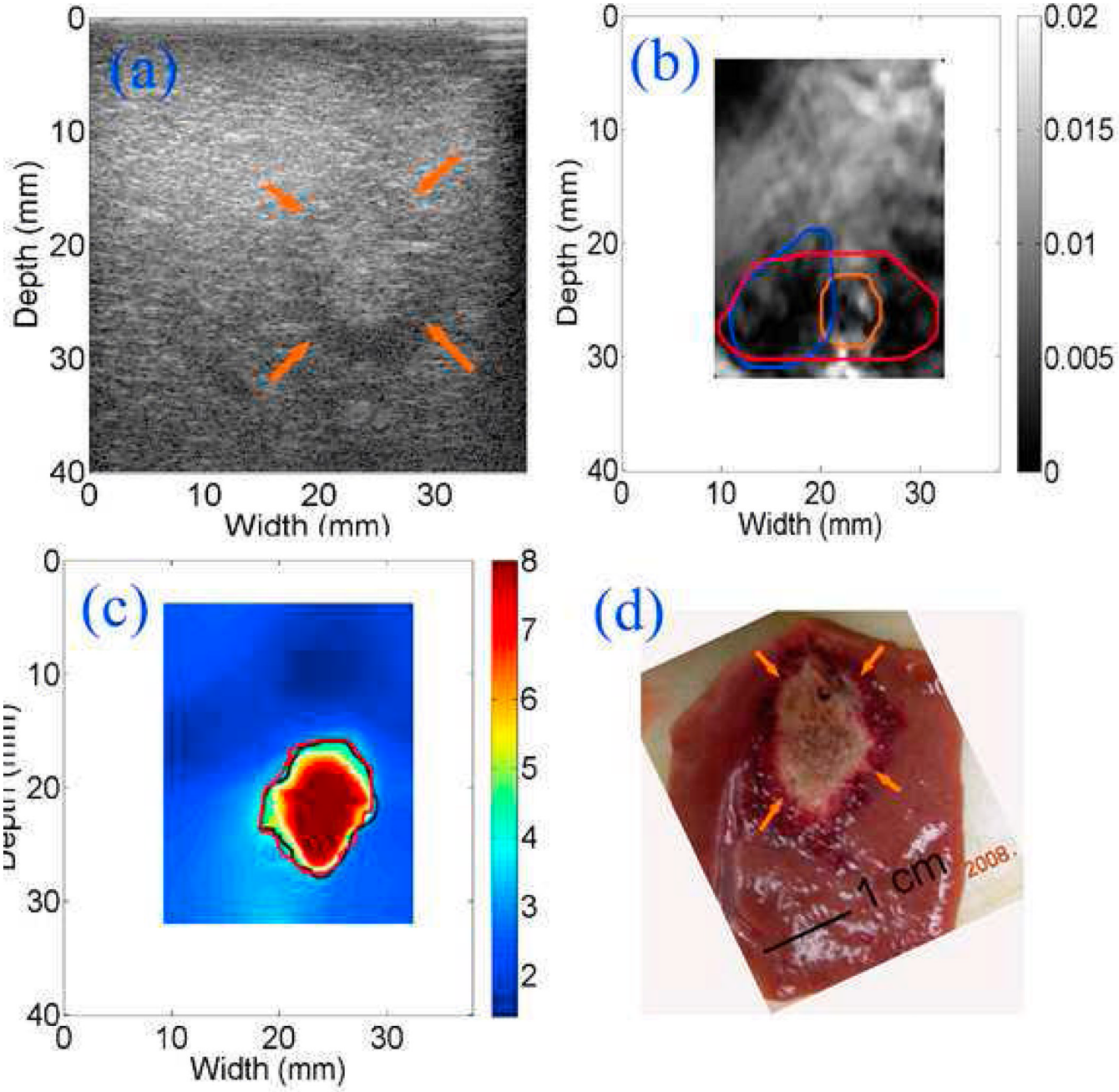

Fig. 10.

Images of an in vivo thermal ablation zone: (a) B-mode, (b) strain, (c) reconstructed relative elastic modulus and (d) photography of gross pathology. The contours on (b) and (c) were replicas of human observers' boundaries of ablation zones. Arrows in (a) and (d) point to the thermal ablation zone.